RMetS
Royal Meteorological Society

A dynamical ocean feedback mechanism for the Madden–Julian Oscillation

Benjamin G. M. Webber[a]*, Adrian J. Matthews[a,b] and Karen J. Heywood[a]
[a] *School of Environmental Sciences, University of East Anglia, Norwich, UK*
[b] *School of Mathematics, University of East Anglia, Norwich, UK*
*Correspondence to: Benjamin G. M. Webber, School of Environmental Sciences, University of East Anglia, Norwich, NR4 7TJ, UK. E-mail: b.webber@uea.ac.uk

Composite analysis is applied to study the dynamical ocean response to Madden–Julian (MJ) events, measured by anomalies in sea surface height from the merged TOPEX/Poseidon–European Remote Sensing satellite altimetry dataset. In each of the tropical ocean basins, significant equatorial waves are forced, which are shown to modulate the sea surface temperature (SST) by 0.2–0.3 °C in the absence of strong surface heat fluxes. In the Indian Ocean there is a clear dynamical response which may play a significant role in generating later MJ events. Surface westerly winds, associated with the active phase of the Madden–Julian Oscillation (MJO), force an eastward-propagating oceanic downwelling equatorial Kelvin wave, which, on reaching the eastern boundary at Sumatra, forces reflected downwelling equatorial Rossby waves and coastal Kelvin waves. The coastal Kelvin waves propagate southwards towards northern Australia and northwards into the Bay of Bengal, and will be important for local physical, chemical and biological processes. The equatorial Rossby waves propagate westward across the Indian Ocean, arriving in the western Indian Ocean approximately 80–100 days after the initial Kelvin wave was generated. The arrival of these waves generates positive SST anomalies which leads to convection and may trigger the next-but-one MJ event, or amplify the low-frequency tail of the MJO. This constitutes a coupled feedback mechanism from the ocean dynamics onto the MJO, somewhat similar to the delayed oscillator mechanism for the El Niño Southern Oscillation. Copyright © 2010 Royal Meteorological Society

Key Words: MJO generation mechanism; equatorial Kelvin waves; equatorial Rossby waves; Indian Ocean dynamics; intraseasonal variability; delayed oscillator

Received 24 August 2009; Revised 16 December 2009; Accepted 10 February 2010; Published online in Wiley InterScience 21 April 2010

Citation: Webber BGM, Matthews AJ, Heywood KJ. 2010. A dynamical ocean feedback mechanism for the Madden–Julian Oscillation. *Q. J. R. Meteorol. Soc.* **136**: 740–754. DOI:10.1002/qj.604

1. Introduction

At intraseasonal time-scales, the Madden–Julian Oscillation (MJO) is the primary source of tropical atmospheric variability. It consists of eastward-propagating regions of enhanced and suppressed convection and rainfall, associated with baroclinic wave structures evident in the wind and pressure fields (Madden and Julian, 1971, 1972). The MJO is a quasi-periodic occurrence with a broad spectral signal. It is typically defined by a period of ∼30–60 d but is associated with convective variability over a broader spectral range (Salby and Hendon, 1994), including scale interactions with high-frequency convection (Majda and Biello, 2004; Batstone *et al.*, 2005). The MJO is most active in the warm pool of the Indian Ocean and the western Pacific, but it modulates atmospheric variability globally (Matthews *et al.*, 2004; Donald *et al.*, 2006), with significant impacts on rainfall, agriculture and business. Zhang (2005) and Lau and Waliser (2005) provide full reviews of the MJO.

The MJO forces a substantial thermodynamic response in the surface layers of the ocean (Jones *et al.*, 1998; Woolnough *et al.*, 2000; Waliser *et al.*, 2003). Within the warm pool, the anomalous surface winds of the MJO combine with climatological surface westerlies to produce an asymmetrical total wind speed signature that is enhanced (suppressed) during westerly (easterly) anomalies. These winds lead to variations in the latent heat flux from the ocean, which is closely related to wind speed. The short-wave flux is also modulated by cloud cover during the MJO: the enhanced (suppressed) convective phase leads to a reduction (increase) in short-wave flux and thus cooling (warming).

Therefore, when there is active convection over the central Indian Ocean, the reduced latent heat flux warms the eastern Indian Ocean while the reduced short-wave and increased latent heat fluxes cool the western Indian Ocean, potentially leading to enhancement (reduction) of convection to the east (west) and thus eastward propagation. The reverse process may account for the eastward propagation of the subsequent suppressed convective anomalies. The surface fluxes combine to generate sea surface temperature (SST) variability of ∼0.15–0.35 °C (Shinoda *et al.*, 1998), which precede the convective anomalies by a quarter of a cycle, consistent with a potential feedback between the two (Flatau *et al.*, 1997; Woolnough *et al.*, 2000).

There remains considerable debate over the relative importance of this oceanic thermodynamic coupling compared with other, atmospheric-only mechanisms which have also been suggested to explain the MJO. These mechanisms include atmospheric instability linked to frictional moisture convergence (Hendon and Salby, 1994), the interaction between convection and atmospheric Kelvin and Rossby waves (Matthews, 2000), external forcing from the midlatitudes (Hsu *et al.*, 1990), and internal atmospheric multiscale interactions (Majda and Biello, 2004). However, coupled models generally perform better at simulating the MJO than atmosphere-only models, although the degree of improvement varies from minimal (Hendon, 2000) to more substantial (Inness and Slingo, 2003). Additionally, intraseasonal SST anomalies can force realistic atmospheric MJO behaviour in atmosphere-only models (Woolnough *et al.*, 2001; Fu and Wang, 2004; Matthews, 2004). It is therefore clear that there is at least the potential for SST anomalies to be a key component of the MJO, but that many such mechanisms will likely be important to the MJO at different times.

Near the Equator, low-frequency planetary-scale Kelvin and Rossby waves are a key component of the oceanic dynamics and energy budget. Equatorial Kelvin waves have typical wavelengths of the order of 10 000–15 000 km (Kessler *et al.*, 1995), with typical sea surface height (SSH) perturbations of ∼10 cm (Giese and Harrison, 1990). The propagation speed of both Kelvin and Rossby waves depends upon the vertical structure of the waves (their 'baroclinic mode') and the stratification of the background state through which they propagate.

Equatorial Kelvin waves are non-dispersive. Depending on the mean stability profile, typical theoretical wave speeds are in the range $c_e = 2.4\text{–}3.0\,\mathrm{m\,s^{-1}}$ for the first baroclinic mode (Chelton *et al.*, 1998). Equatorial Rossby waves follow the dispersion relation

$$c = \frac{-\beta}{k^2 + (2n+1)\beta/c_e},$$

where $\beta \approx 2.3 \times 10^{-11}\mathrm{m^{-1}s^{-1}}$ is the meridional gradient of planetary vorticity, k is the zonal wavenumber, and n is the meridional mode. Long Rossby waves (with small k) are non-dispersive, with phase speed $c = -c_e/(2n+1)$. Rossby waves with wavelengths of the order of half the width of the Indian Ocean basin are weakly dispersive, with phase speeds reduced relative to the long-wave value by approximately 15%. The meridional scale of equatorial Kelvin and Rossby waves is determined by the equatorial Rossby radius of deformation, $R = (c_e/\beta)^{1/2}$.

Kelvin and Rossby waves perturb the thermocline depth by three orders of magnitude more than they perturb the SSH. Waves with a positive SSH signal correspond to a deeper thermocline and are thus termed 'downwelling' waves. Conversely, waves with a negative SSH signal correspond to upwelling. Kelvin waves have a meridional structure of SSH and zonal current with a single maximum (or minimum) at the Equator. In contrast, there are multiple meridional structures for equatorial Rossby waves, the simplest being the symmetrical $n = 1$ meridional mode wave which has maxima (or minima) at 2–5°N and 2–5°S (Chelton *et al.*, 2003).

The surface zonal wind anomalies of the MJO are one mechanism by which Kelvin and Rossby waves are generated. Battisti (1988) showed that a symmetric equatorial westerly wind burst generates downwelling Kelvin waves and upwelling Rossby waves through the Ekman divergence field, although the response is dependent on the meridional structure of the wind field. Downwelling waves deepen the thermocline and raise the SST by reducing the entrainment of cold subsurface waters, while upwelling waves lead to enhanced entrainment and cooling (McCreary, 1983). The SST may also be modified by zonal and meridional advection, which may be of first-order importance in regions where a strong temperature gradient exists (Philander, 1981). Thus, the dynamical oceanic response to the MJO has the potential to generate SST anomalies which then feed back onto the atmosphere. Although the primary cause of intraseasonal SST variability within the region where the MJO is active comes from the surface fluxes, dynamical forcing still plays a substantial role and may locally contribute up to 50% of the total forcing (Waliser *et al.*, 2003).

In the eastern Pacific Ocean, the first baroclinic mode equatorial Kelvin wave period is observed to be around 70 d. Although this is longer than the dominant period of the MJO, the MJO is broadband with spectral power extending to ∼95 d (Salby and Hendon, 1994). In addition, closer examination of Kelvin waves forced by the MJO shows a transient decline in phase speed during periods of enhanced MJO activity, which would reduce the observed frequency of the waves in the eastern Pacific and may thus account for the frequency difference between the waves and the MJO (Roundy and Kiladis, 2006). The eastward propagation of the forcing allows resonance to occur, so that the MJO will more efficiently generate such waves than stationary wind bursts (Hendon *et al.*, 1998). The MJO-induced waves remotely force SST fluctuations of more than 0.5 °C (Zhang, 2001), deepen the thermocline by as much as 50 m (Kessler *et al.*, 1995) and play a role in the generation and amplification of El Niño events (Kessler *et al.*, 1995; McPhaden, 1999; Edwards *et al.*, 2006).

Outside of the Pacific Ocean, the dynamical response to the MJO has been less well studied. Katz (1997) showed that Kelvin waves in the Atlantic have an intraseasonal periodicity of ∼40–60 d, consistent with the time-scale of the MJO. However, the predominant forcing mechanism for these waves was found to be the seasonal cycle in the trade winds. Han *et al.* (2008) found that the primary cause of Atlantic intraseasonal variability in SSH and SST was Kelvin wave activity forced by local wind variability. They noted that this local variability may be remotely influenced by the MJO (Foltz and McPhaden, 2004), as well as by convective variability in the Amazon basin, but did not conclusively show evidence for an interaction with the MJO.

In the Indian Ocean, MJO-related Kelvin and Rossby wave variability has been observed at multiple time-scales; intraseasonal spectral peaks have been found at 45 and 90 d (Han *et al.*, 2001), as well as lesser peaks at 70, 62.5 and 58.8 d (Fu, 2007). The 90 d peak appears to be the preferred time-scale of the ocean dynamics and may enhance atmospheric variability on such time-scales (Han *et al.*, 2001). The spectral peaks are strongest at around 4–5° north and south of the Equator, consistent with equatorial Rossby wave structures (Chelton *et al.*, 2003). The MJO is known to interact with the Indian Ocean Dipole (IOD; e.g. Saji *et al.*, 1999) through the ocean dynamics; Rao and Yamagata (2004) showed that Kelvin waves forced by the MJO can terminate IOD events. In addition, Shinoda and Han (2005) found that submonthly variability in the central and eastern Indian Ocean, which is correlated with the IOD, can force an equatorial Kelvin wave response which may then feed back to the IOD by modulating the SST. Nevertheless, the interaction between the dynamics of the Indian Ocean and the MJO remains poorly understood.

The MJO undergoes a strong seasonal cycle; it is most coherent during boreal winter when it propagates zonally along the Equator, while during boreal summer there is more northward propagation and interaction with the Asian monsoon (Wang and Rui, 1990). This seasonal cycle affects the dynamical response, which will be most efficiently generated by the zonally propagating, equatorial component of the MJO. In addition, the frequency of the MJO is influenced by seasonality (Pohl and Matthews, 2007), with implications for the resonant amplification of the ocean waves.

There evidently remains much scope for studying ocean dynamics over the MJO life cycle. This study elucidates the dynamic ocean response by using a compositing technique to study the time and phase evolution of SSH and SST in relation to the MJO. The use of satellite altimetry to study the MJO life cycle through composites is novel; previously the focus has generally been the connection between the MJO and the El Niño Southern Oscillation (ENSO) in the Pacific (Edwards *et al.*, 2006), or on studying intraseasonal ocean dynamics in the Indian Ocean but without reference to the phase-by-phase evolution of the MJO (Han *et al.*, 2001; Han, 2005; Fu, 2007). Various atmospheric fields are studied to investigate atmosphere–ocean interaction and feedbacks, including the potential for the MJO-forced dynamical waves to modulate the SST and feed back onto the MJO convection. Section 2 describes the datasets used in this study and section 3 outlines the methodologies used. The results are presented in section 4, starting with the global response and then focusing on the Pacific, Atlantic and Indian Oceans. The conclusions are discussed in section 5.

2. Data

The merged TOPEX/Poseidon–Earth Remote Sensing (T/P–ERS) satellite altimetry dataset is used for the SSH analysis (Fu *et al.*, 1994). This was chosen in preference to the TOPEX/Poseidon data alone since the combination of multiple satellite datasets enhances spatial resolution and improves variance (Ducet *et al.*, 2000; Le Traon *et al.*, 2001), although there is a slight decrease in effective temporal resolution (Greenslade *et al.*, 1997). The 'reference' dataset, which is a homogeneous dataset based on two satellites with the same groundtrack, is used as opposed to the 'updated' one, which uses up to four satellites at a given time. This sacrifices the potential for enhanced accuracy with improved satellite coverage in order to maintain consistent sampling in time. The data were obtained on a 0.25° grid as weekly maps for the period from 14 October 1992 to 23 January 2008, and then interpolated using cubic splines to daily values. SST data were obtained from the Tropical Microwave Imaging (TMI) satellite (Kummerow *et al.*, 2000). The data used are daily maps of the 3-day average SST at 0.25° resolution for the period of 1 January 1998 to 17 December 2008.

Outgoing long-wave radiation (OLR) data from the Liebmann and Smith (1996) dataset are used as a proxy for convective activity and rainfall. The dataset is optimally interpolated onto a 2.5° grid and in this study the daily mean data from 1 January 1990 to 31 October 2008 are used. Surface (10 m) wind data were obtained from the European Centre for Medium-range Weather Forecasts (ECMWF) interim analysis for the period from 1 January 1998 to 1 January 2009. The surface fluxes of latent heat, sensible heat, short-wave radiation and long-wave radiation were obtained from the ECMWF ERA-40 reanalysis for the period from 1 January 1998 to 1 January 2002, and from the ECMWF operational forecasts for the period 2 January 2002 to 31 December 2008.

The linear trend and annual cycle are calculated pointwise for each variable, then the mean, trend and first three harmonics of the annual cycle are subtracted from the data to produce detrended anomaly fields. These are then bandpass-filtered using a 20–200 d Lanczos filter. This broadband filter has been shown to efficiently exclude both high-frequency noise and low-frequency climate signals while retaining the MJO signal and preserving the distinction between individual MJ events better than a narrower (e.g. 30–70 d) filter (Matthews, 2000). The filter uses 241 symmetric weights, meaning that 120 d of data are lost at each end of the dataset. All datasets are further truncated so that an integer number of calendar years of data are retained, thus avoiding seasonal bias. Note that very similar results were obtained when the data were not filtered.

3. Methodology

The Wheeler–Hendon (WH) index (Wheeler and Hendon, 2004) is used to track MJO activity. This index is based on a multi-variate principal component analysis of high-pass filtered OLR and zonal winds at 850 and 200 hPa. The index is produced in real time, retains a high proportion of temporally coherent variance in the 30–80 d range and is independent of season. Every day is assigned to one of the eight phases defined by the two principal components (RMM1 and 2) of the index. Phase 1 corresponds to minimum convection over the Maritime Continent and the initiation of active convective anomalies in the western Indian Ocean. These anomalies move eastwards in each successive phase; by phase 4 the positive convective anomalies overlie the Maritime Continent while the suppressed convection has propagated into the western Pacific. A new region of suppressed convection originates in the western Indian Ocean at phase 5; phases 5–8 are thus equivalent to phases 1–4 with anomalies of the opposite sign.

The WH index is becoming an accepted way to track MJO activity and has been used by many MJO studies since it was introduced (Donald *et al.*, 2006; Pohl and Matthews, 2007; Matthews, 2008). However, as with any index of the MJO, it will include variability with different modes of behaviour and time-scales, such that the results will depend slightly on the definition of the MJO. Note that the WH index does contain variability not associated with the MJO, especially atmospheric Kelvin waves which can contribute substantially (Roundy *et al.*, 2009); however, the compositing technique used here should reduce the impact of such noise unless that noise systematically varies in response to the MJO in a way which projects onto the oceanic response.

To investigate this oceanic response, composites are created separately for each MJO phase, using all days within that phase when the amplitude of the WH index exceeds an arbitrary threshold value of 1.5. This value was chosen to select the stronger MJO events (whose impact on the ocean should be stronger and more coherent), as opposed to the threshold value of 1 chosen by Wheeler and Hendon (2004). Composites for a given phase are generated by taking the mean of the composited field over all days that lie within that MJO phase and exceed the threshold.

Since an average MJO cycle takes ∼48 d, each phase lasts for ∼6 d. However, this can vary greatly depending on the MJ event (Salby and Hendon, 1994), as well as season and ENSO phase (Pohl and Matthews, 2007). This variation means that signals analysed with respect to phase can represent a combination of events with different individual lifetimes. Therefore, although the eight MJO phase composites provide a robust picture of the evolution of the MJO in a particular variable, the exact time dependence of these signals is uncertain. Hence, time-lagged composites are also generated by adding or subtracting a set number of days from all these dates. These represent a more accurate and robust method for evaluating the time evolution of the physical processes, and tend to produce more accurate estimates of phase speed than compositing on MJO phase (Matthews *et al.*, 2009).

The resulting composite anomaly fields are tested for local (grid-point) significance at the 95% level using a resampling technique (Wilks, 1995). The histogram of the null distribution for this test is generated at each grid point from 1000 Monte Carlo simulations. Each simulation consists of a composite which has the same number of MJ events, each with the same length as the original, but where these events are randomly selected. The dates of the events maintain seasonality through the constraint of lying within 15 d of the original composite calendar date, but are freely chosen from any year. Note that since the resampling technique is a non-parametric test, it is not necessary for the the number of degrees of freedom to be explicit in the formulation. However, this number is implicitly assumed to be the number of MJ events and remains constant throughout the simulations.

Each grid point value for each composite is then tested for local significance at the 95% level by comparison with the 2.5th and 97.5th percentile values of the null distribution. Field significance is also tested for each composite by generating a null distribution of the fractional area of the map that is locally significant at the 95% level from the Monte Carlo simulations. By definition, this distribution has a mean value of 5% but spatial correlations tend to increase the spread and skewness of the distribution such that the 95th percentile often exceeds 10%, especially when the test is done over a smaller area. For a map of composite anomalies to pass the field significance test, the fraction of the map which is locally significant must exceed this value. This would be expected whenever there is a genuine physical process occurring, since the true response will be added to the 5% of anomalies expected to be present by chance.

4. The dynamic ocean response

4.1. *Global response*

As an overview of the global dynamic ocean response to the MJO, the SSH anomalies in phase 8, at lag 0, are shown in Figure 1. At this phase of the MJO, suppressed convective anomalies are located over the Maritime Continent, leading to surface easterly wind anomalies over the Indian Ocean (not shown). The band of significant negative SSH anomalies along the Equator in the Indian Ocean indicates the presence of an upwelling equatorial Kelvin wave being forced by these overlying easterlies. The off-equatorial SSH maxima near the coast of Sumatra indicate a downwelling Rossby wave generated by reflection of a downwelling Kelvin wave earlier in the MJO cycle (section 4.4), although this will be further amplified by the concurrent wind forcing. The preceding Kelvin wave has also forced downwelling coastal Kelvin waves which can be seen propagating around the Bay of Bengal and southwards along the coast of Java. These waves will advect temperature and energy polewards, away from the warm pool. There is also evidence of energy propagation into the Indonesian seas, notably through the Sunda channel between Java and Sumatra, which may affect the variability of the Indonesian Throughflow.

In the equatorial Pacific, a full Kelvin wave (both positive and negative anomalies) can clearly be seen, with maximum SSH perturbations of ±2–3 cm. The timing of the positive SSH anomalies (indicating downwelling) is consistent with the local forcing by the MJO in the western Pacific, but the magnitude of the negative anomalies (indicating upwelling) in the central Pacific, where there is no local forcing, demonstrates the potential for the MJO to remotely influence the local dynamics.

In the Atlantic Ocean there is a weak (<1 cm) but significant upwelling (negative SSH anomalies) Kelvin wave apparent at the Equator, in addition to positive SSH anomalies along the coast and along 5°S. These latter anomalies are possibly due to coastal Kelvin and reflected Rossby waves respectively, generated by the downwelling Kelvin wave forced by the preceding MJ event.

In general, the extratropical anomalies are weaker and less coherent than the equatorial anomalies. However, there are spatially (and temporally; not shown) coherent regions of significantly negative SSH anomalies in both the

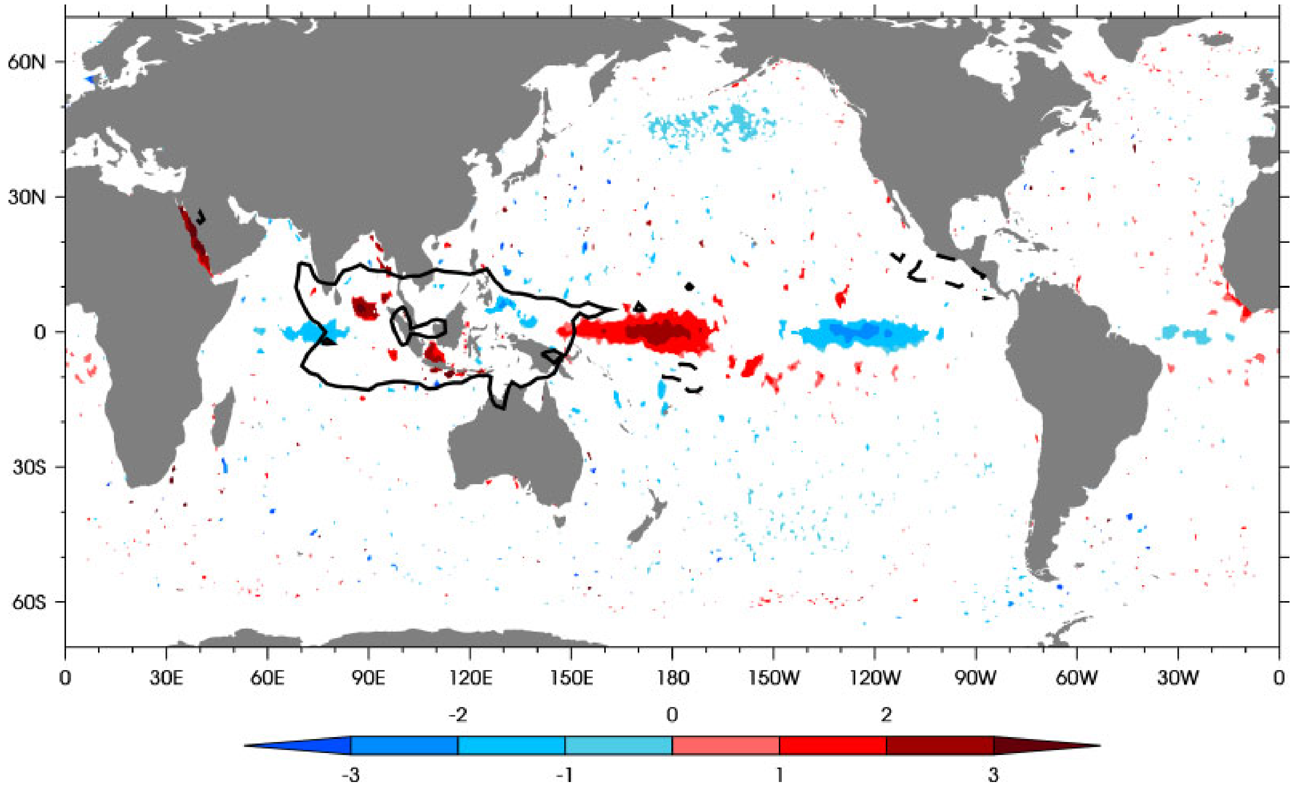

Figure 1. Composite anomalies of sea surface height for phase 8 lag 0. The contour and shading interval is 1 cm. Regions where the anomalies are not significant at the 95% level are masked such that only significant anomalies are visible. OLR is plotted as thick contours at ±10 W m^{-2}; the negative contour is dashed. This composite passes the field significance test at the 95% confidence level. This figure is available in colour online at www.interscience.wiley.com/journal/qj

North and South Pacific, near 50°N and 50°S respectively. It may be that these anomalies are associated with the atmospheric extratropical response to the MJO, which drives significant surface wind variability on the MJO time-scale (e.g. Matthews *et al.*, 2004; Matthews and Meredith, 2004; Donald *et al.*, 2006). Another possible cause is the interaction between the MJO and high-frequency transient waves in the subtropical jets (Matthews and Kiladis, 1999). However, a detailed analysis of the extratropical response to the MJO is beyond the scope of this paper. Here, we will focus on the tropical oceanic response.

4.2. *Pacific Ocean*

Because the dynamic response of the Pacific Ocean to the MJO has been well studied in relation to the link with ENSO (e.g. Kessler *et al.*, 1995; McPhaden, 1999; Edwards *et al.*, 2006), it is useful to compare our composites with previous studies to provide a benchmark with which results presented later in this paper may be compared. Composites, time lagged with respect to phase 2 of the MJO, are shown in Figure 2. At lag 0, the downwelling (positive SSH anomalies) Kelvin wave present in the western Pacific in the phase 8 composite (Figure 1) has propagated eastward into the central Pacific, with maximum SSH anomalies of over 3 cm (Figure 2(a)). Phase 2 of the MJO represents a transition phase with suppressed convection propagating into the western Pacific accompanied by underlying easterly anomalies. The relationship between the atmospheric forcing and the oceanic response can be clearly seen as these easterly anomalies start to force a new, upwelling, Kelvin wave, which propagates to the central Pacific 20 d later (Figure 2(b)). At this time, the downwelling Kelvin wave has reached the coast of South America where it is subsequently transformed into coastal Kelvin waves. Downwelling Kelvin waves have been observed by the Tropical Atmosphere Ocean (TAO) buoy array to deepen the thermocline of the eastern Pacific and interrupt the thermal influence of climatological upwelling, potentially triggering El Niño events (Kessler *et al.*, 1995; McPhaden, 1999; Roundy and Kiladis, 2006).

The propagation speed of the Kelvin waves can be estimated from the composites; the downwelling wave is originally centred at around 140°W, reaching 100°W 20 d later. Thus its speed is approximately 2.6 m s^{-1}, consistent with the theoretical Kelvin wave speed for this region of 2.4–2.6 m s^{-1} (Chelton *et al.*, 1998, their Figure 2). Previous theoretical and observational studies have suggested wave speeds nearer 2.3–2.4 m s^{-1} (Hendon *et al.*, 1998), but considering the uncertainty involved in estimating the Kelvin wave speed from only two composites, this is well within the reasonable range of values. In general, the results presented here are in good agreement with those from previous studies, suggesting that the methodology is valid.

4.3. *Atlantic Ocean*

Intraseasonal Kelvin waves in the Atlantic Ocean have been observed in response to the seasonal cycle (Foltz and McPhaden, 2004; Han *et al.*, 2008), but no conclusive link with the MJO has been found. Here, we examine the strength and coherence of the dynamic response to the MJO in our composites. In addition, the Atlantic Ocean represents an ocean basin without strong thermodynamic forcing by the

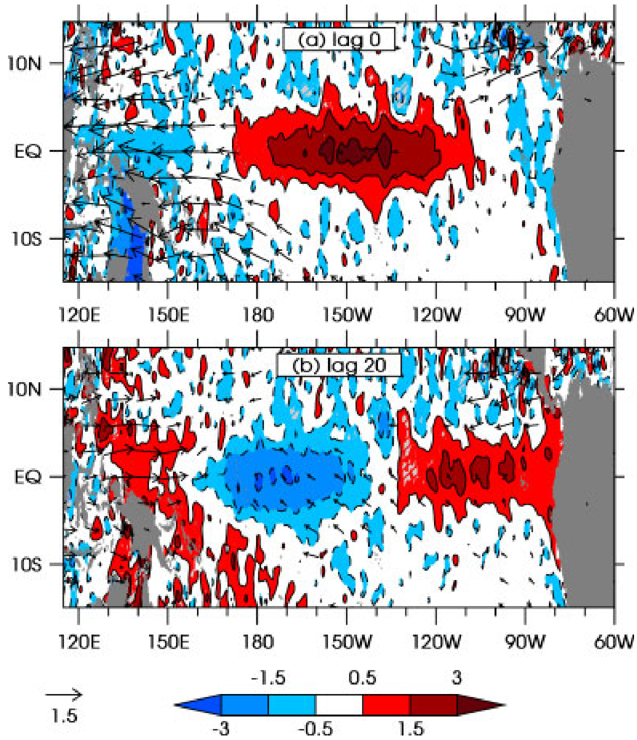

Figure 2. Composite anomalies of sea surface height (cm) for (a) phase 2 lag 0 and (b) phase 2 lag 20 d in the tropical Pacific. The shading and contour intervals are shown in the legend. Regions where the anomalies are not significant at the 95% level are hatched over such that only significant anomalies are clearly visible. Surface winds are plotted where either the u- or v-component is significant at the 95% confidence level; a scale vector of 1.5 m s^{-1} is shown. All composites pass the field significance test at the 95% confidence level. This figure is available in colour online at www.interscience.wiley.com/journal/qj

MJO and is thus a good test of the strength of the dynamically induced SST anomalies.

In addition to the upwelling equatorial Kelvin wave in the Atlantic at phase 8 (Figure 1), there is a downwelling equatorial Kelvin wave which occurs at phase 3, lag 0 (Figure 3). Although the magnitude of the SSH anomalies is only a third of those seen in the Pacific, the wave is nevertheless significant and temporally coherent at other lags (not shown). The negative SSH anomalies along the African coast to the north and south are possibly due to the upwelling coastal Kelvin waves forced by the upwelling equatorial Kelvin wave shown in Figure 1. The significant wind anomalies are weak and do not coincide with the location of the Kelvin wave, implying weak wind stress. However, there is a broad region of westerly anomalies at phase 2 (not shown), which is likely to be the source of the downwelling Kelvin wave shown here.

The weakness of the wind and OLR anomalies also implies minimal surface flux anomalies of latent heat and short-wave radiation, allowing the relationship between the dynamical waves and the concurrent SST anomalies to be clearly seen (Figure 3(b)). Because downwelling waves deepen the thermocline and reduce entrainment, the downwelling equatorial wave leads to positive SST anomalies along the Equator, while the upwelling coastal Kelvin wave is associated with cold anomalies. The SST anomalies correspond almost exactly with the location of the Kelvin waves, peak at over 0.2 °C, and are significant at the 95% confidence level. Thus the remote response to the MJO in the Atlantic Ocean is substantial and drives SST fluctuations of the same order of magnitude as the flux-driven SST variability in the warm pool (Shinoda *et al.*, 1998).

4.4. *Indian Ocean*

4.4.1. *Annual average*

We now focus on the Indian Ocean response, which is a key region of interest because it lies entirely within the core region of MJO activity. Therefore, any dynamically induced SST anomalies will have a direct effect on the MJO. In addition, the Maritime Continent reflects a large proportion of incoming Kelvin wave energy as equatorial Rossby waves. The remainder of the incoming energy will be split between northward- and southward-propagating coastal Kelvin waves. The southward component will escape into the Pacific but the northward component cannot propagate through the shallow Malacca Strait between Sumatra and Malaysia and will thus propagate around the northern boundary of the basin. Therefore, in contrast to the Pacific, the majority of the wave energy will not radiate away from the forcing, but will instead remain trapped within the Indian Ocean, with the potential for resonant coupling between the MJO and the dynamical response.

Figure 4 shows the SSH response in the Indian Ocean for all eight phases of the MJO, with the concurrent OLR and surface wind anomalies overlaid. The upwelling equatorial Kelvin wave generated by the easterly anomalies at phase 8 (Figure 1 and Figure 4(h)) reaches the coast of Sumatra by phase 1 (Figure 4(a)) where it triggers upwelling coastal Kelvin waves. These waves propagate polewards over the subsequent phases. The southward component propagates along the coasts of Sumatra and Java and then continues into the Indonesian seas, thus escaping the Indian Ocean. The northward-propagating coastal Kelvin wave circumnavigates the Bay of Bengal by phase 3, when a narrow region of negative SSH anomalies can be seen along the east coast of India. At phase 4, negative anomalies can be seen on the western coast of India, indicating that the coastal Kelvin wave has propagated around the tip of India and into the Arabian seas.

At phase 3, a first meridional mode ($n = 1$) equatorial Rossby wave is generated by reflection of the incoming Kelvin wave at the eastern boundary, indicated by the dual SSH minima at 2–5°N and S. The westerly wind anomalies at phases 3 and 4 also generate positive wind stress curl which will lead to anomalous upwelling by Ekman divergence and then amplify and extend the reflected wave. This equatorial Rossby wave propagates westward, reaching the longitude of the tip of India at phase 5. The northern part of the Rossby wave interacts with the coastal Kelvin wave, amplifying the negative anomalies along the western coast of India. At phase 7, the easterly wind anomalies weaken the equatorial Rossby waves and generate a new upwelling equatorial Kelvin wave, at which point the cycle begins again.

In addition to this cycle in the upwelling waves, there is an equivalent cycle in the downwelling (positive SSH anomaly) waves. The downwelling equatorial Kelvin wave is forced at phase 4, transforms into coastal Kelvin waves at phase 5, which themselves circumnavigate the Bay of Bengal before coinciding with reflected Rossby waves at the tip of India at phase 1. The Rossby waves continue to propagate westwards, initially amplified by the easterly winds until the westerly

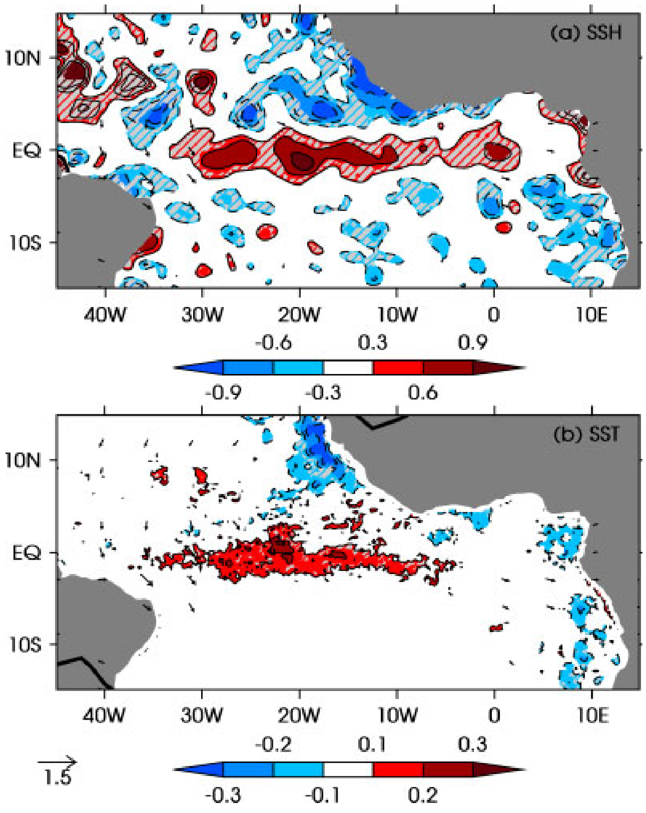

Figure 3. Composite anomalies of (a) sea surface height (b) sea surface temperature for phase 3 lag 0 of the MJO in the tropical Atlantic. The shading and contour interval is (a) 0.3 cm and (b) 0.1 °C. Surface winds are plotted where either the *u*- or *v*-component is significant at the 95% confidence level; a scale vector of 1.5 m s^{-1} is shown. Regions where the anomalies are not significant at the 95% level are hatched over such that only significant anomalies are clearly visible. OLR is plotted as thick contours at ±10 W m^{-2}; the negative contour is dashed. All composites pass the field significance test at the 95% confidence level. This figure is available in colour online at www.interscience.wiley.com/journal/qj

winds which begin at phase 3 reduce their amplitude and force the new downwelling equatorial Kelvin wave at phase 4. Thus, the cyclical nature of the MJO can be clearly seen in the composites of the dynamical ocean response, which are roughly inverted half a cycle later (compare the left- and right-hand panels of Figure 4).

The coastal Kelvin waves propagating around the Bay of Bengal will affect the local upwelling and the coastal currents; for example there is known to be intraseasonal variability in the East India Coastal Current (Durand *et al.*, 2009), which is likely to be partly due to such waves. The subsequent propagation along the west coast of India supports the findings of Vialard *et al.* (2009) that variability in current velocities near 15°N, 73°E is dominated by strong intraseasonal variability induced by coastal Kelvin waves similar to those found here and forced by the equatorial winds of the MJO.

This timing and interaction of the various waves forced by the surface winds is similar to that found by Valsala (2008) in an idealised modelling study of the oceanic response to seasonal variability using a patch of equatorial zonal wind stress. The similarity of the results shows that similar oceanic mechanisms are important for modulating the oceanic response to the seasonal cycle and the MJO. However, the shorter time-scale of the MJO allows a different resonance to occur. As discussed above, the reflected upwelling equatorial Rossby wave generated at phase 3 is amplified by the reversal of the MJO-induced surface winds to westerlies during phases 4–5 and the resulting pattern of equatorial convergence and off-equatorial divergence. Similarly, the surface easterlies amplify the reflected downwelling waves at phases 7–1. In contrast, the longer-lived seasonal forcing would continue to enhance the equatorial Kelvin waves and suppress the reflected equatorial Rossby waves.

The Kelvin waves appear to be generated in the central Indian Ocean rather than the western part. This is likely due both to the relative weakness of the wind anomalies in the western Indian Ocean and resonant amplification between the eastward-propagating forcing and the oceanic Kelvin waves, similar to that found in the Pacific by Hendon *et al.* (1998). These waves continue to amplify upon arrival at the coast of Sumatra as easterly wind anomalies along the Equator and southeasterly anomalies along the coast of Sumatra continue to generate upwelling. As the enhanced convective anomalies of the MJO propagate into the Maritime Continent from phase 2 to phase 4, the Indian Ocean wind anomalies weaken and then reverse, at which point a downwelling equatorial Kelvin wave begins to form. A similar mechanism amplifies this downwelling Kelvin wave at phase 5 before the winds reverse again at phase 6.

In addition to the waves clearly evident in the equatorial Indian Ocean, there is a significant and cyclical response in the Red Sea, with positive anomalies during phases 7 to 1, and negative anomalies during phases 3 to 5. The anomalies peak at over ±3 cm and appear to be a response to the local wind forcing which reverses from northwesterly in phase 3 to southeasterly in phase 7. It is plausible that this represents net transport in response to the intraseasonal winds, but the quality of the altimetry dataset may be questionable within a narrow and shallow region such as the Red Sea.

While the composites by MJO phase (Figure 4) give a robust overview of the main features of the dynamical ocean

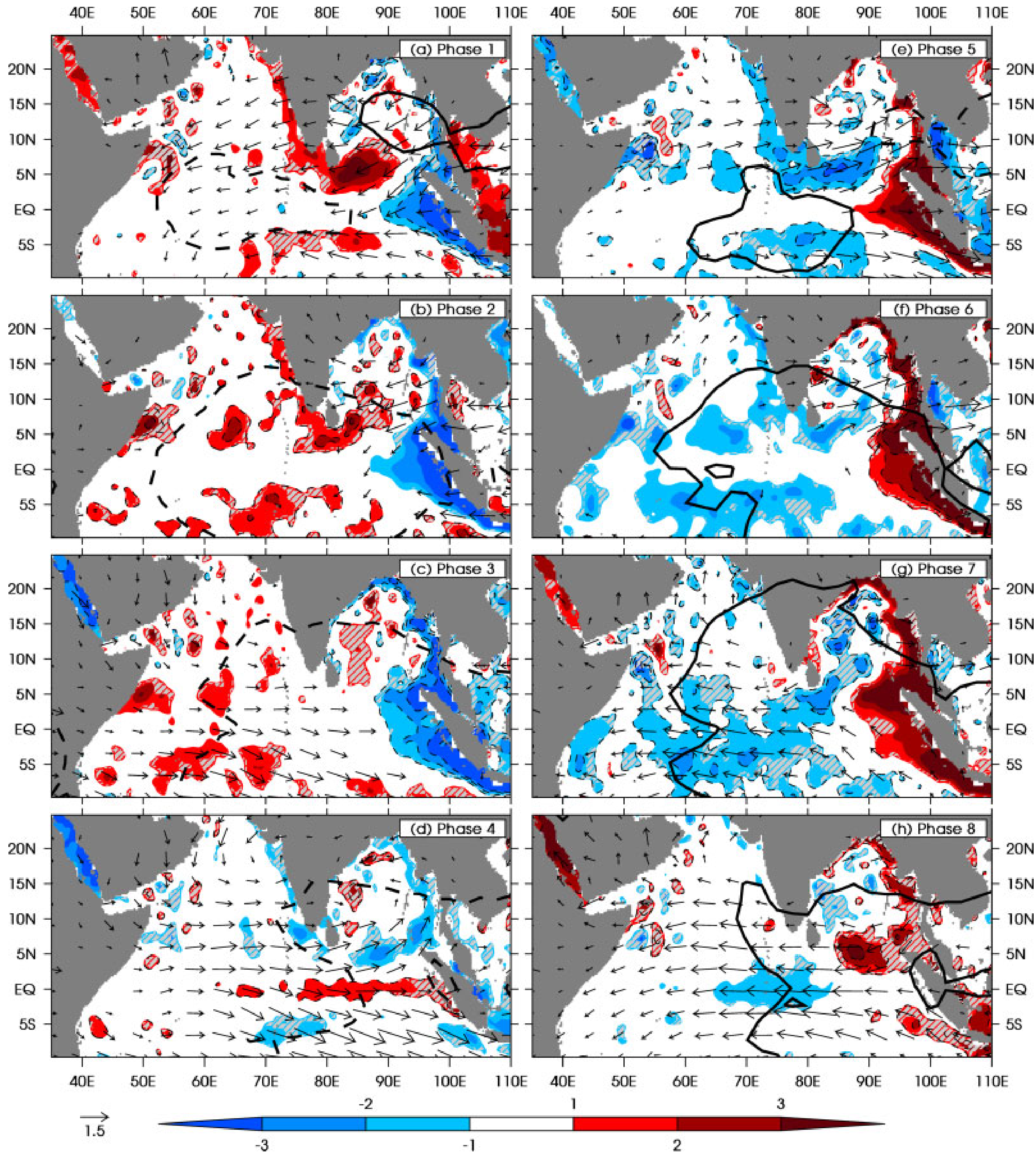

Figure 4. Composite anomalies of sea surface height for all eight phases of the MJO. The contour and shading interval is 1 cm. Regions where the anomalies are not significant at the 95% level are hatched over such that only significant anomalies are clearly visible. Surface winds are plotted where either the *u*- or *v*-component is significant at the 95% confidence level; a scale vector of 1.5 m s^{-1} is shown. OLR is plotted as thick contours at ±10 W m^{-2}; the negative contour is dashed. All composites pass the field significance test at the 95% confidence level. This figure is available in colour online at www.interscience.wiley.com/journal/qj

response to the MJO, the broadband nature of the MJO means that it is not possible to accurately calculate phase speeds for the waves, nor to study their time evolution in detail. To investigate this further, Figure 5 shows time lag composites of SSH and SST lagged with respect to phase 1. The positive SSH anomalies of the downwelling equatorial Rossby wave originate at lag –30 (Figure 5(a)) in the eastern Indian Ocean when the downwelling Kelvin wave generated during the previous MJO cycle reflects at the Sumatran coast. This corresponds approximately to the MJO phase 5 panel in Figure 4(e). The positive SSH anomalies can then be tracked as they propagate westwards through to lag 60, when they reach the coast of Africa. Hence there is a 90 d time-scale from the oceanic Rossby wave propagation, which is twice the 45 d time-scale of the canonical MJO.

Given the cyclical anomalies shown in Figure 4, it might be expected that the SSH anomalies at lag 0 (Figure 5(a)) would be repeated after a full cycle of the MJO, i.e. around lag 50 (Figure 5(h)). However, this is not the case, consistent with the ocean dynamics having a different time-scale to the forcing. Indeed, the Rossby wave signal does not arrive in the western Indian Ocean until lag 60, implying that the positive SSH anomalies in this region in the MJO phase maps (Figure 4(c)) are the aliased signal from the arrival of Rossby waves a full MJO cycle after they were forced. The difference in time-scales between the intraseasonal dynamics of the Indian Ocean and the MJO has been noted by Han *et al.* (2001) and Han (2005), who suggested that the shift is due to a resonant response of the equatorial Indian Ocean at the 90 d time-scale.

In Figure 5, the relationship between the SSH and SST anomalies is generally weak, compared with the close correlation for the Atlantic composites shown in Figure 3. This is perhaps unsurprising given the strength of the surface flux anomalies associated with the MJO in the Indian Ocean. The total flux anomaly is primarily composed of the shortwave and latent heat fluxes (Woolnough *et al.*, 2000), so it is possible to make qualitative estimates of the strength of the total flux from the strength of the OLR and wind anomalies. The wind anomalies are generally stronger in the eastern Indian Ocean, and decrease in magnitude and significance with time, becoming largely insignificant by lag 60. The OLR anomalies are strong at lags 0 and 10 but rapidly decrease in magnitude later, with few anomalies exceeding the contour value of $\pm 7.5\,\mathrm{W\,m^{-2}}$. By lag 60, the relationship between SST and SSH becomes stronger and more coherent, with positive anomalies around 50–60°E, and a broad region of negative anomalies between 70 and 100°E. The arrival of the Rossby waves and the associated positive SST anomalies near 60°E may help to trigger convection over the Indian Ocean 60 d after it was previously active in phase 1.

To investigate this hypothesised relationship, we construct lagged Hovmöller diagrams of SSH, SST and total accumulated surface heat flux for the Indian Ocean. The maximum amplitude SSH anomalies associated with first meridional mode equatorial Rossby waves occur off the Equator between 2 and 5°N/S (Chelton *et al.*, 2003). Since this is consistent with the waves seen in the composites, we create the SSH Hovmöller diagrams by averaging over these latitude ranges to isolate the Rossby wave response. This method produces similar results to averaging over each latitude band separately, implying that the Rossby waves present in the lagged composites have a symmetric, meridional mode 1 structure with dual maxima, as opposed to higher meridional modes which are either anti-symmetric or have a more complex structure (Chelton *et al.*, 2003).

Because both the MJO activity and the mean circulation in the Indian Ocean undergo a strong seasonal cycle, the summer and winter monsoon seasons were analysed separately. This allows the effects of the equatorial currents on the Rossby wave phase speed to be investigated further and allows the impact of such variation on the atmosphere–ocean feedbacks to be examined.

4.4.2. Northern winter

Figure 6 shows the Hovmöller diagrams of SSH and SST for all MJO events occurring between November and April (the northeast monsoon). Both the upwelling and downwelling Rossby waves can clearly be seen on Figure 6(a). The downwelling Rossby wave, forced by Kelvin waves generated in the previous MJ event, propagates from around 90°E at lag –20 to 50°E around lag 45, in time for the next MJ event. This implies a phase speed of roughly $0.8\,\mathrm{m\,s^{-1}}$, shown by the solid line in Figure 6.

Figure 6(b) shows the SST Hovmöller diagram, which displays little in the way of propagation. The SST anomalies tend to follow the surface fluxes with the canonical quarter-cycle lag (Shinoda *et al.*, 1998, as discussed in section 1). However, it is likely that the propagation of the downwelling Rossby wave (shown by the diagonal line in Figure 6) will also raise the SSTs slightly such that the warm (cool) anomalies are amplified (reduced), but that this is largely masked by the flux-induced SSTs. In addition, the thermocline is deeper in the central and eastern Indian Ocean such that the effect of upwelling on SSTs will be reduced.

A key result of this study is that the arrival of the downwelling Rossby wave in the western Indian Ocean leads to a local increase of the SST with the potential to trigger a new MJ event. In Figure 6, there is an extended region of anomalously high SSTs at 55–60°E between lags 40 and 50, occurring shortly after the Rossby wave has propagated through this region. These high SSTs cannot be attributed to surface fluxes since the total fluxes are negative for ∼12 d prior to the SST maximum, thus they are most likely generated by the Rossby wave. The western Indian Ocean is known to be a region in which there is a relatively high correspondence between thermocline depth and SST; Xie *et al.* (2002) show that the maximum correlation occurs in a region 3–10°S, 50–80°E.

These SST anomalies near 60°E at lag 50 are at least as strong and coherent as those in the same location at lag 0, and roughly equivalent to the thermodynamic response to the MJO (Shinoda *et al.*, 1998). Note that the relative modesty of these SST anomalies is partly due to the compositing methodology, which, by averaging over a large number of events, will tend to reduce the magnitude of any individual anomalies. Intraseasonal SST anomalies of this magnitude have been shown to force MJO convection in atmosphere-only models (Fu and Wang, 2004; Matthews, 2004), and, if SSTs in the western Indian Ocean are important for initiating the MJO convection, then the dynamically induced SST anomalies at lag 50 could be sufficient to generate a new MJ event. However, the anomalies further east around lag 35 are more zonally coherent and will also contribute to the generation of the next MJ cycle. It should be stressed that the initiation of a new MJ event by the Rossby wave-induced SSTs is one of many possible generation mechanisms which may all influence the behaviour of the MJO. Nevertheless, this proposed mechanism will contribute to the broadband nature of the MJO by enhancing the longer time-scale variability.

To investigate the response of the MJO to these dynamically forced SST anomalies, Hovmöller diagrams of OLR anomalies have been constructed for the same period. Because the MJO-induced OLR anomalies are meridionally extensive, the anomalies are averaged over a latitude range of 8°S–8°N such that the OLR anomalies accurately represent MJO activity. Constructing the Hovmöller diagrams over the same latitude bands as for the SSTs does not alter the relationship between OLR and SST substantially for either summer or winter, but merely results in a stronger agreement between the two fields (not shown). Figure 7(a) shows the OLR composite for November–April. The MJO is strongly cyclical across the basin, with a period of around 40 d. The eastward-propagating anomalies of the MJO originate around 40–50°E at lag 0, but originate further east at lag 50,

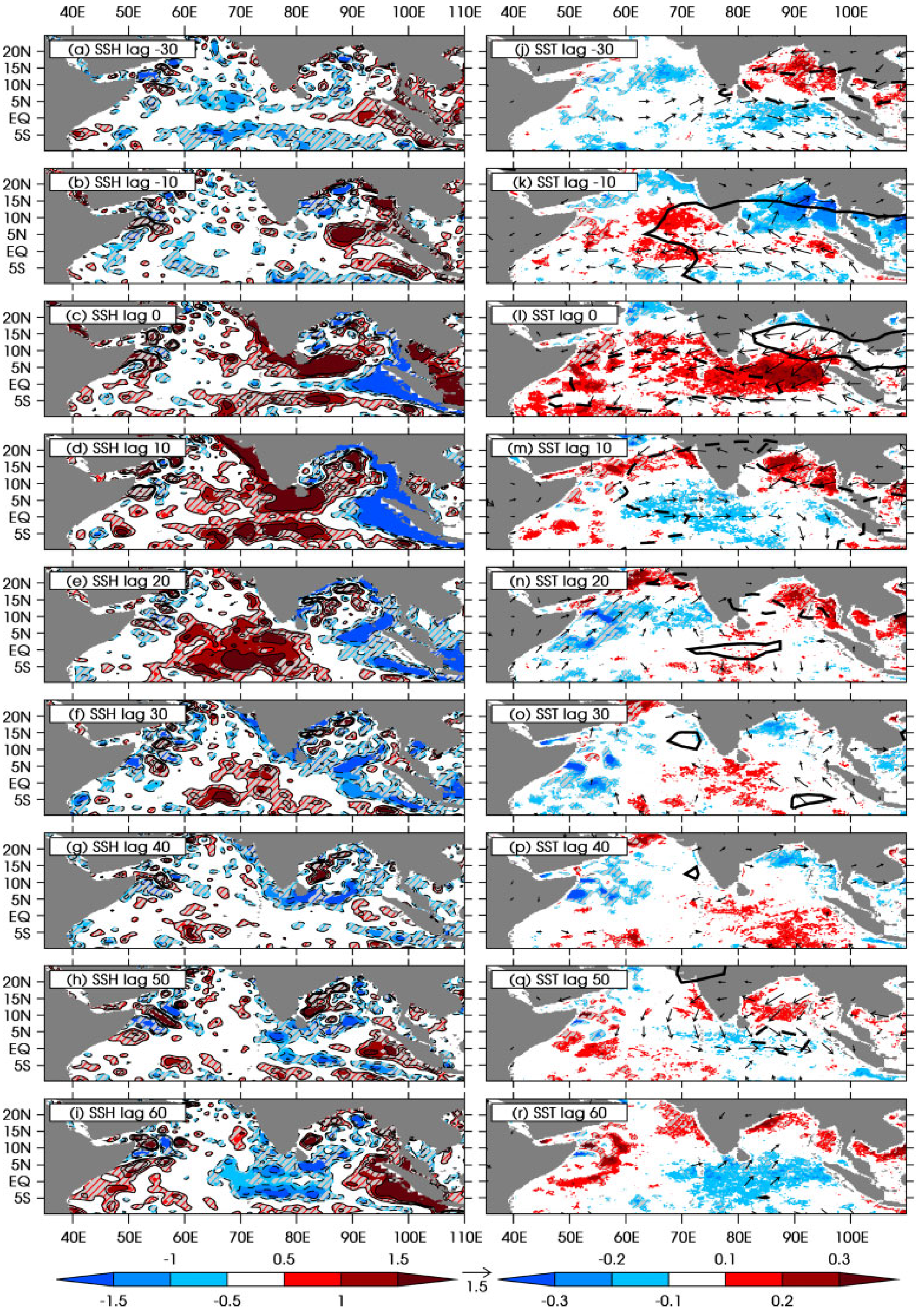

Figure 5. Composite anomalies of (a)–(i) sea surface height (cm) and (j)–(r) sea surface temperature (°C) at lags –30, –10, 0, 10, 20, 30, 40, 50 and 60 d relative to phase 1 of the MJO. Surface winds are plotted where either the *u*- or *v*-component is significant at the 95% confidence level; a scale vector of 1.5 m s^{-1} is shown. For (a)–(i), the contour and shading interval is 0.5 cm, and for (j)–(r) the shading interval is 0.1 °C. OLR is plotted as thick contours at ±7.5 W m^{-2} in (j)–(r); the negative contour is dashed. Regions where the anomalies are not significant at the 95% level are hatched over such that only significant anomalies are clearly visible. The SSH composites at lags 0, 10, 20, 30 and 60 and the SST composites at lags –30, –10, 0, 10, 20, 40 and 60 pass the field significance test at the 95% confidence level This figure is available in colour online at www.interscience.wiley.com/journal/qj

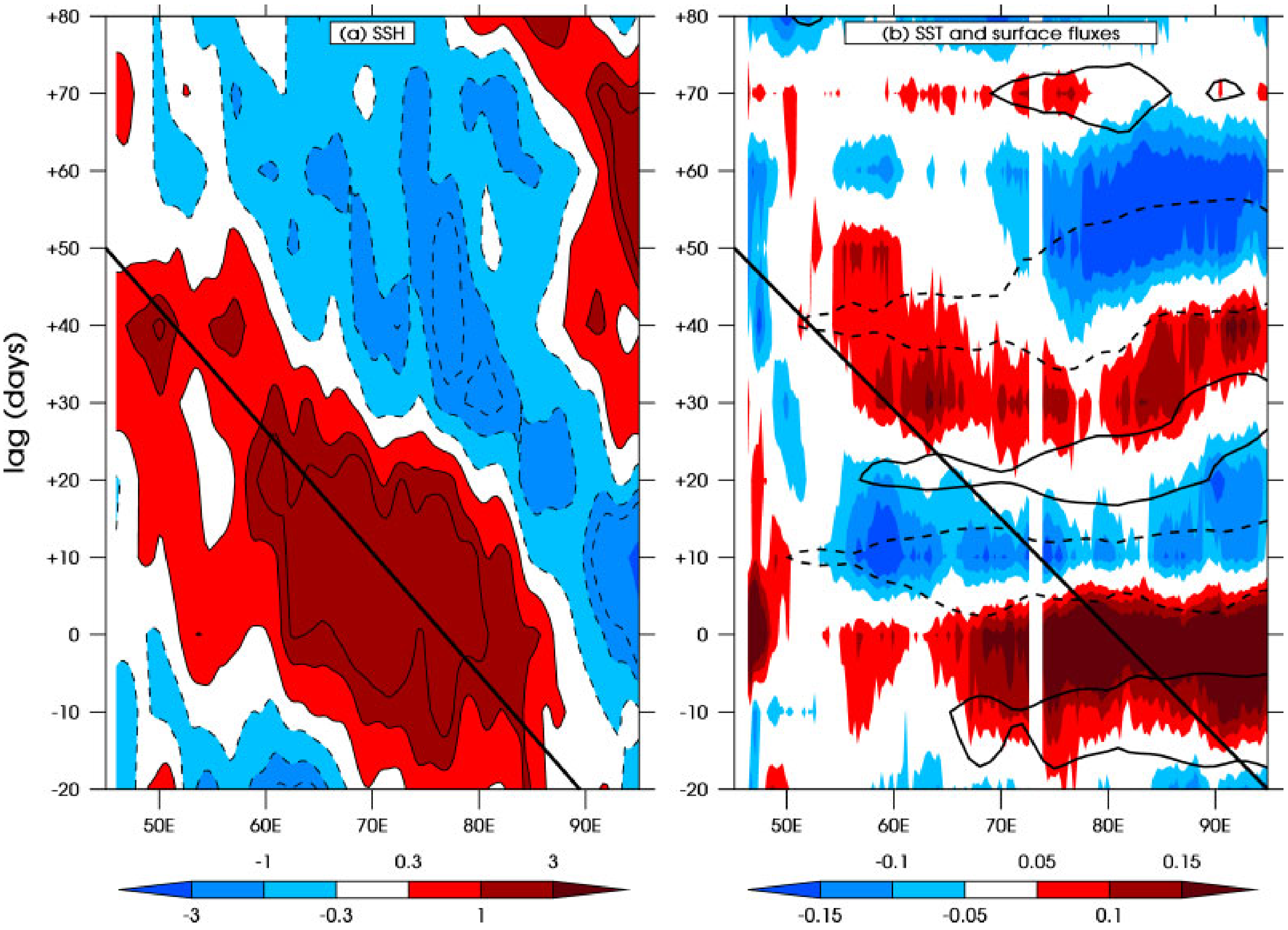

Figure 6. Hovmöller diagram of (a) composite SSH anomalies and (b) composite SST anomalies for lags –20 to 80 relative to phase 1 of the MJO, averaged between 2 and 4°N and 2 and 4°S for November–April. The shading interval is as shown in the legends in cm and °C, respectively. In (b), the total surface heat flux is contoured at 12 W m^{-2}, the negative contour is dashed, and the zero contour is omitted. The solid diagonal lines represent the propagation of the downwelling Rossby wave in (a). This figure is available in colour online at www.interscience.wiley.com/journal/qj

when the MJO is initiated at the same longitude as the dynamically induced SST anomalies.

From the data available it is hard to determine the relative importance of this dynamical mechanism compared with other mechanisms for generating subsequent MJO events, especially during the winter monsoon season when the various mechanisms coincide. The feedback from the dynamical waves onto the MJO is likely to be a source of resonant amplification in this season. The importance of the mechanism can be partly tested by comparison of the behaviour of the MJO in different seasons.

4.4.3. Northern summer

Figure 8 shows the Hovmöller diagram of SST and SSH for the southwest monsoon period between May and October. The propagation speed for the Rossby wave is somewhat lower; the positive SSH anomalies do not reach the western Indian Ocean until lag 70 implying a phase speed of 0.7 m s^{-1}. In comparison, the theoretical first internal mode Rossby wave speed for non-dispersive Rossby waves in the Indian Ocean is 0.9 m s^{-1} (Chelton *et al.*, 2003; Fu, 2007). However, as noted in the introduction, for Rossby wavelengths of the order of 20–30° longitude there is an error of ∼15% relative to the non-dispersive approximation, reducing the phase speed to 0.68–0.77 m s^{-1}. Another possible reason for the discrepancy is the meridional potential vorticity (PV) gradient, which Chelton *et al.* (2003) showed reduced the phase speed of non-dispersive equatorial Rossby waves in the Pacific by ∼0.2 m s^{-1}.

In addition, the equatorial currents in the Indian Ocean exhibit a strong seasonal cycle which is likely to have an effect on the phase speed of the equatorial Rossby waves. In northern summer, there is a broad, eastward mean current with velocities of the order of 0.2–0.3 m s^{-1}, which will reduce the Rossby wave phase speed. In northern winter the current structure is more complex with a westward North Equatorial Current of 0.3 m s^{-1} in the eastern Indian Ocean and 0.5–0.8 m s^{-1} in the western region, and an eastwards Equatorial Countercurrent of 0.5–0.8 m s^{-1} (Tomczak and Godfrey, 1994). The total mean current between roughly 5°N and 5°S is therefore considerably less in northern winter, becoming negligible in January. Doppler shifting by the mean currents is thus consistent with the lower Rossby wave phase speed in summer. However, the relatively narrow meridional width of equatorial currents means that the change in the Rossby wave phase speed is often considerably less than the magnitude of the current velocities (McPhaden and Ripa, 1990). Quantifying this and the effect of changes to the stratification and the meridional PV gradients requires further research and is beyond the scope of this study.

Consistent with the hypothesis that the Rossby waves generate positive SSTs upon reaching the western Indian Ocean, the timing of the SST anomalies around 55°E is closely related to the SSH anomalies. There is a similar

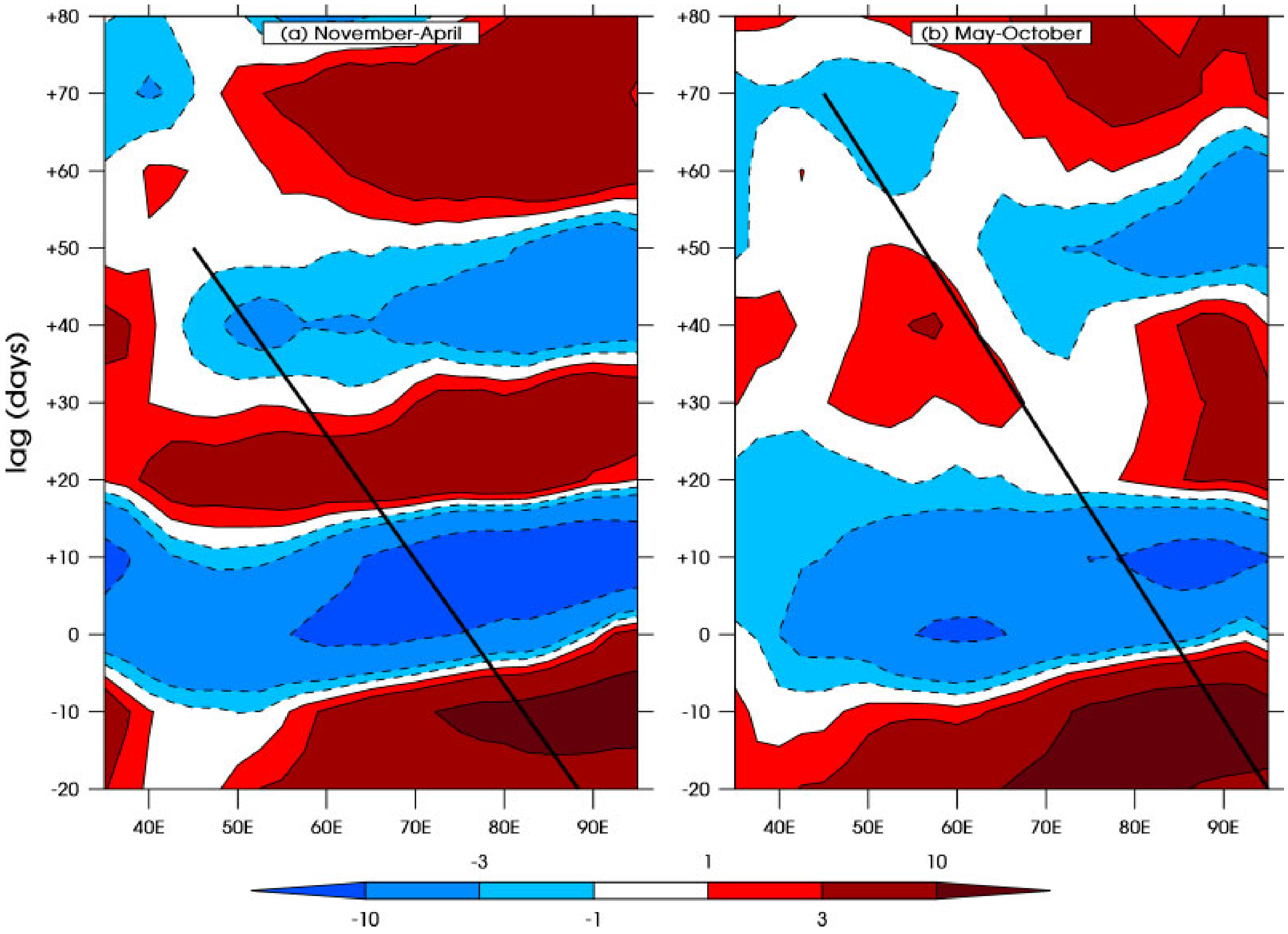

Figure 7. Hovmöller diagram of OLR anomalies for lags –20 to 80 relative to phase 1 of the MJO, for (a) November–April and (b) May–October. The contour and shading interval is shown in the legend (in W m^{-2}). The solid diagonal lines represent the propagation of the downwelling Rossby waves in (a) November–April and (b) May–October. This figure is available in colour online at www.interscience.wiley.com/journal/qj

time lag between the Rossby wave propagation and the SST anomalies as seen for the winter monsoon. Further east, the SST variability appears more closely related to the surface fluxes, although modulation by the Rossby wave is also apparent.

During northern summer, positive SST anomalies of over 0.15 °C are present around 55°E between lags 50 and 80, comparable in magnitude to those present at zero lag, and equal to the overall magnitude of SST variation in response to the MJO in the Indian Ocean (Shinoda *et al.*, 1998). These SSTs do not have a coherent phase relationship with the local surface fluxes, in contrast to the SST anomalies in the central Indian Ocean which exhibit the canonical quarter-cycle lag described in section 1. Thus, the dynamically forced SSTs of the western Indian Ocean would act to enhance MJO variability at periods of 60–70 d, or shift the initiation region further eastwards. We note that the eastward-propagating MJO is generally less coherent during boreal summer, and speculate that this delaying mechanism may be (at least partly) the cause.

The OLR composite for the summer monsoon (May–October, Figure 7(b)) is strikingly different from that for the winter monsoon. The period of the MJ events is longer, consistent with the longer transit times for the Rossby waves. Although the second composite MJ event occurs before the arrival of the Rossby waves in the western Indian Ocean, it originates further east, around 70°E, closely following the arrival of the Rossby wave at this longitude. In addition, there is evidence of westward-propagating OLR anomalies overlying the Rossby waves from lags 50–70, indicating an interaction between the two processes. There is also potential for the arrival of the Rossby waves in the western Indian Ocean to trigger MJ events around lag 70, which would enhance the low-frequency component of the MJO, although the Hovmöller diagram (Figure 7(b)) suggests that this is less common.

5. Conclusions

This study has shown the magnitude of the global dynamical response to the MJO, which includes significant anomalies in all tropical ocean basins and remote responses in the extratropics. That these remotely forced responses are significant is indicative of the sensitivity of the ocean to the MJO; in addition, the locally forced anomalies are long lived and temporally coherent, remaining significant out to lags of 60 d in the Indian Ocean.

In addition, this paper has highlighted the role of the ocean dynamics as a component of the coupled MJO system within the Indian Ocean, where a strong response is evident in the ocean dynamics which subsequently lead to SST anomalies with the potential to feed back to the atmosphere. This relationship between the ocean dynamics and SST is similar to that found by Shinoda and Han (2005), who showed that submonthly variability enhanced by the IOD forces equatorial Kelvin waves which feed back onto

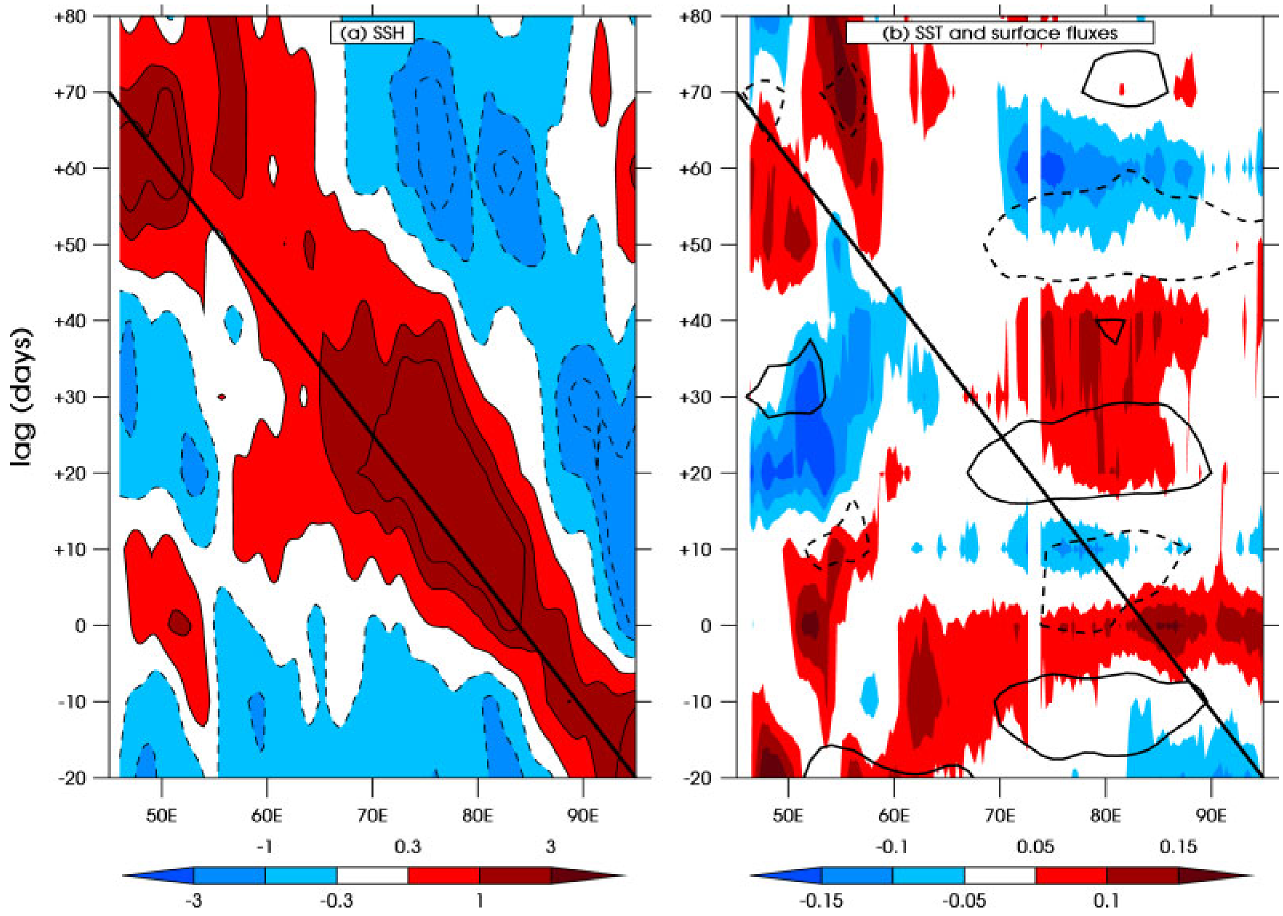

Figure 8. As Figure 6, but for May–October. This figure is available in colour online at www.interscience.wiley.com/journal/qj

the atmosphere through anomalous downwelling and thus higher SSTs along the coast of Sumatra. The magnitude of the SST anomalies found here is equivalent to those forced by the surface fluxes of the MJO (Shinoda *et al.*, 1998), which have been shown to force atmospheric convection similar to the MJO in atmospheric models (Fu and Wang, 2004; Matthews, 2004).

The key components of this proposed feedback mechanism are summarised in Figure 9. The westerly surface wind anomalies associated with phases 3–4 of the MJO generate a downwelling equatorial Kelvin wave. This subsequently reflects into a downwelling equatorial Rossby wave which propagates westwards and arrives in the western Indian Ocean around 90 d after the initial Kelvin wave was forced, although this time-scale will vary with season due to the different Rossby wave propagation speeds.

The timing of the Rossby wave arrival in the western Indian Ocean will, when the MJO is periodic with a time-scale of 48 d, approximately coincide with the next-but-one MJ event. Alternatively, there may be no intervening event, in which case this mechanism is a potential trigger for primary MJ events (Matthews, 2008). In either case, this mechanism will amplify the low-frequency component of the MJO, and may also modulate its seasonality. The mechanism is reminiscent of the delayed oscillator theory of ENSO (Battisti, 1988), although the time-scale is very different, partly due to the much smaller ocean basin.

Despite the importance of the flux-driven SST anomalies in the central and eastern Indian Ocean, the SST anomalies in the western Indian Ocean are of equal magnitude but are clearly driven by the Rossby waves. This is highlighted by the difference in the SST fields between the summer and winter monsoons. This variation can be explained by the difference in the Rossby wave propagation speed which is consistent with the seasonal cycle in equatorial currents, suggesting that Doppler shifting is of first-order importance. The SST anomalies cannot be explained by local surface fluxes, since the two fields are almost exactly out of phase. Indeed, it appears that the surface flux variations in this region are primarily driven by short-wave flux variations (implied by the OLR anomalies) in *response* to the SSTs. Note that these convective anomalies in the western Indian Ocean will be important for the local and East African climate whether or not they generate a new MJ event.

The response of the MJO to the dynamic ocean forcing is complicated by the other mechanisms which sustain the MJO; for example, the composite Hovmöller diagrams (Figures 6, 7 and 8) indicate that the new MJ event is most likely to occur when both the dynamic and thermodynamic SST forcings are positive. In the winter monsoon (November–April), these two factors combine at around lag 40 to create a strongly cyclical MJO which is initiated in the western Indian Ocean. In contrast, for the summer monsoon composites, these two factors are in phase in the central Indian Ocean, from where the convective anomalies originate. The arrival of the Rossby waves in the western Indian Ocean does appear to generate convection in summer, but this is out of phase with the other forcing mechanisms such that this mechanism will reduce the coherence but increase the broadband nature of the summer MJO.

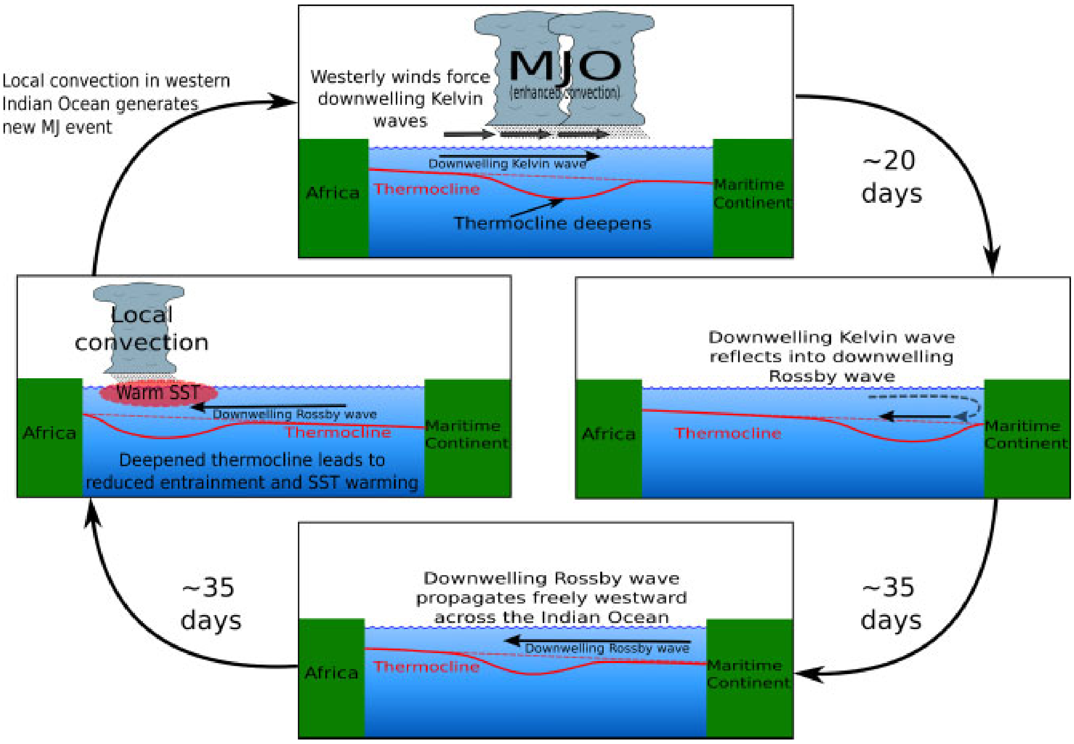

Figure 9. Schematic of MJO dynamical ocean feedback mechanism. This figure is available in colour online at www.interscience.wiley.com/journal/qj

Our results imply that, to accurately model the MJO, the ocean dynamics may need to be simulated adequately enough to resolve the Kelvin and Rossby waves as well as the SST anomalies forced by these waves. Achieving this may resolve some of the current difficulties with modelling the MJO (Inness and Slingo, 2003). The significance of the dynamical response has implications for the circulation, chemistry and biology of the tropical oceans. Further work is necessary to investigate such matters, in addition to determining the strength of the feedback onto the MJO. It is hoped that this paper has highlighted the importance of these questions, the answers to which may help improve our understanding of the coupled MJO system.

Acknowledgements

The merged TOPEX/Poseidon–ERS-1 satellite altimetry data were provided by AVISO and are available on their website at http://www.aviso.oceanobs.com/. The TMI SST data were obtained from the SSM/I website at http://www.ssmi.com/tmi/. The EMCWF winds and surface flux data were obtained through the British Atmospheric Data Centre (BADC) and from the ECMWF website at http://data-portal.ecmwf.int/data/d/interim_daily/. The interpolated OLR data were obtained from the NOAA/OAR/ESRL PSD web site at http://www.cdc.noaa.gov/. The Wheeler–Hendon index was obtained from http://www.bom.gov.au/. The authors thank Paul Roundy and an anonymous reviewer for comments which helped to improve the manuscript. BGMW was supported by a NERC PhD studentship.

References

Batstone CP, Matthews AJ, Stevens DP. 2005. Coupled ocean–atmosphere interactions between the Madden–Julian oscillation and synoptic-scale variability over the warm pool. *J. Climate* **18**: 2004–2020.

Battisti DS. 1988. Dynamics and thermodynamics of a warming event in a coupled tropical atmosphere ocean model. *J. Atmos. Sci.* **45**: 2889–2919.

Chelton DB, DeSzoeke RA, Schlax MG, El Naggar K, Siwertz N. 1998. Geographical variability of the first baroclinic Rossby radius of deformation. *J. Phys. Oceanogr.* **28**: 433–460.

Chelton DB, Schlax MG, Lyman JM, Johnson GC. 2003. Equatorially trapped Rossby waves in the presence of meridionally sheared baroclinic flow in the Pacific Ocean. *Prog. Oceanogr.* **56**: 323–380.

Donald A, Meinke H, Power B, Maia ADN, Wheeler MC, White N, Stone RC, Ribbe J. 2006. Near-global impact of the Madden-Julian oscillation on rainfall. *Geophys. Res. Lett.* **33**: L09704, DOI: 10.1029/2005GL025155.

Ducet N, Le Traon PY, Reverdin G. 2000. Global high-resolution mapping of ocean circulation from TOPEX/Poseidon and ERS-1 and -2. *J. Geophys. Res.* **105**: 19477–19498.

Durand F, Shankar D, Birol F, Shenoi SSC. 2009. Spatio-temporal structure of the East India Coastal Current from satellite altimetry. *J. Geophys. Res.* **114**: C02013, DOI: 10.1029/2008JC004807.

Edwards LA, Houseago-Stokes RE, Cipollini P. 2006. Altimeter observations of the MJO/ENSO connection through Kelvin waves. *Int. J. Remote Sens.* **27**: 1193–1203.

Flatau M, Flatau P, Phoebus P, Niiler PP. 1997. The feedback between equatorial convection and local radiative and evaporative processes: The implications for intraseasonal oscillations. *J. Atmos. Sci.* **54**: 2373–2386.

Foltz GR, McPhaden MJ. 2004. The 30–70 day oscillations in the tropical Atlantic. *Geophys. Res. Lett.* **31**: L15205, DOI: 10.1029/2004GL020023.

Fu LL. 2007. Intraseasonal variability of the equatorial Indian Ocean observed from sea surface height, wind, and temperature data. *J. Phys. Oceanogr.* **37**: 188–202.

Fu LL, Christensen EJ, Yamarone CA, Lefebvre M, Menard Y, Dorrer M, Escudier P. 1994. TOPEX/Poseidon mission overview. *J. Geophys. Res.* **99**: 24369–24381.

Fu XH, Wang B. 2004. Differences of boreal summer intraseasonal oscillations simulated in an atmosphere-ocean coupled model and an atmosphere-only model. *J. Climate* **17**: 1263–1271.

Giese BJ, Harrison DE. 1990. Aspects of the Kelvin wave response to episodic wind forcing. *J. Geophys. Res.* **95**: 7289–7312.

Gill AE. 1982.. *Atmosphere-ocean dynamics*. Academic Press.

Greenslade DJM, Chelton DB, Schlax MG. 1997. The midlatitude resolution capability of sea level fields constructed from single and multiple satellite altimeter datasets. *J. Atmos. Ocean. Tech.* **14**: 849–870.

Han W. 2005. Origins and dynamics of the 90-day and 30–60-day variations in the equatorial Indian Ocean. *J. Phys. Oceanogr.* **35**: 708–728.

Han W, Lawrence DM, Webster PJ. 2001. Dynamical response of equatorial Indian Ocean to intraseasonal winds: Zonal flow. *Geophys. Res. Lett.* **28**: 4215–4218.

Han W, Webster PJ, Lin JL, Liu T, Fu R, Yuan D, Hu A. 2008. Dynamics of intraseasonal sea level and thermocline variability in the equatorial atlantic during 200. *J. Phys. Oceanogr.* **38**: 945–967.

Hendon HH. 2000. Impact of air-sea coupling on the Madden–Julian oscillation in a general circulation model. *J. Atmos. Sci.* **57**: 3939–3952.

Hendon HH, Liebman B, Glick JD. 1998. Oceanic Kelvin waves and the Madden–Julian oscillation. *J. Atmos. Sci.* **55**: 88–101.

Hendon HH, Salby ML. 1994. The life-cycle of the Madden–Julian oscillation. *J. Atmos. Sci.* **51**: 2225–2237.

Hsu HH, Hoskins BJ, Jin FF. 1990. The 1985/86 Intraseasonal Oscillation and the role of the extratropics. *J. Atmos. Sci.* **47**: 823–839.

Inness PM, Slingo JM. 2003. Simulation of the Madden–Julian oscillation in a coupled general circulation model. Part I: Comparison with observations and an atmosphere-only GCM. *J. Climate* **16**: 345–364.

Jones C, Waliser DE, Gautier C. 1998. The influence of the Madden–Julian oscillation on ocean surface heat fluxes and sea surface temperature. *J. Climate* **11**: 1057–1072.

Katz EJ. 1997. Waves along the Equator in the Atlantic. *J. Phys. Oceanogr.* **27**: 2536–2544.

Kessler WS, McPhaden MJ, Weickmann KM. 1995. Forcing of intraseasonal Kelvin waves in the equatorial Pacific. *J. Geophys. Res.* **100**: 10613–10631.

Kummerow C, Simpson J, Thiele O, Barnes W, Chang ATC, Stocker E, Adler RF, Hou A, Kakar R, Wentz F, Ashcroft P, Kozu T, Hong Y, Okamoto K, Iguchi T, Kuroiwa H, Im E, Haddad Z, Huffman G, Ferrier B, Olson WS, Zipser E, Smith EA, Wilheit TT, North G, Krishnamurti T, Nakamura K. 2000. The status of the Tropical Rainfall Measuring Mission (TRMM) after two years in orbit. *J. Appl. Meteorol.* **39**: 1965–1982.

Lau WKM, Waliser DE (eds). 2005. *Intraseasonal variability in the atmosphere–ocean climate system*. Springer-Praxis: Heidelberg, Germany.

Le Traon PY, Dibarboure G, Ducet N. 2001. Use of a high-resolution model to analyze the mapping capabilities of multiple-altimeter missions. *J. Atmos. Oceanic Technol.* **18**: 1277–1288.

Liebmann B, Smith CA. 1996. Description of a complete (interpolated) outgoing longwave radiation dataset. *Bull. Am. Meteorol. Soc.* **77**: 1275–1277.

Madden RA, Julian PR. 1971. Detection of a 40-50 day oscillation in zonal wind in the tropical Pacific. *J. Atmos. Sci.* **28**: 702–708.

Madden RA, Julian PR. 1972. Description of global-scale circulation cells in the tropics with a 40–50 day period. *J. Atmos. Sci.* **29**: 1109–1123.

Majda AJ, Biello JA. 2004. A multiscale model for tropical intraseasonal oscillations. *Proc. Natl. Acad. Sci. USA* **101**: 4736–4741.

Matthews AJ. 2000. Propagation mechanisms for the Madden–Julian oscillation. *Q. J. R. Meteorol. Soc.* **126**: 2637–2651.

Matthews AJ. 2004. Atmospheric response to observed intra-seasonal tropical sea surface temperature anomalies. *Geophys. Res. Lett.* **31**: L14107, DOI: 10.1029/2004GL020474.

Matthews AJ. 2008. Primary and successive events in the Madden–Julian oscillation. *Q. J. R. Meteorol. Soc.* **134**: 439–453.

Matthews AJ, Hoskins BJ, Masutani M. 2004. The global response to tropical heating in the Madden–Julian oscillation during the northern winter. *Q. J. R. Meteorol. Soc.* **130**: 1991–2011.

Matthews AJ, Kiladis GN. 1999. The tropical-extratropical interaction between high-frequency transients and the Madden–Julian oscillation. *Mon. Weather Rev.* **127**: 661–677.

Matthews AJ, Meredith MP. 2004. Variability of Antarctic circumpolar transport and the Southern Annular Mode associated with the Madden–Julian oscillation. *Geophys. Res. Lett.* **31**: L24312, DOI: 10.1029/2004GL021666.

Matthews AJ, Singhruck P, Heywood KJ. 2009. Ocean temperature and salinity cycle in the Madden–Julian oscillation observed by Argo floats. *Clim. Dyn.* DOI: 10.1007/s00382-009-0631-7. Published online.

McCreary JP. 1983. A model of tropical ocean–atmosphere interaction. *Mon. Weather Rev.* **111**: 370–387.

McPhaden MJ. 1999. Genesis and evolution of the 1997–98 El Niño. *Science* **283**: 950–954.

McPhaden MJ, Ripa P. 1990. Wave–mean flow interactions in the equatorial ocean. *Annu. Rev. Fluid Mech.* **22**: 167–205.

Philander SGH. 1981. The response of equatorial oceans to a relaxation of the trade winds. *J. Phys. Oceanogr.* **11**: 176–189.

Pohl B, Matthews AJ. 2007. Observed changes in the lifetime and amplitude of the Madden–Julian oscillation associated with interannual ENSO sea surface temperature anomalies. *J. Climate* **20**: 2659–2674.

Rao SA, Yamagata T. 2004. Abrupt termination of Indian Ocean dipole events in response to intraseasonal disturbances. *Geophys. Res. Lett.* **31**: L19306, DOI: 10.1029/2004GL020842.

Roundy PE, Kiladis GN. 2006. Observed relationships between oceanic Kelvin waves and atmospheric forcing. *J. Climate* **19**: 5253–5272.

Roundy PE, Schreck III CJ, Janiga MA. 2009. Contributions of convectively coupled equatorial Rossby waves and Kelvin waves to the real-time multivariate MJO indices. *Mon. Weather Rev.* **137**: 469–478.

Saji N, Goswami B, Vinayachandran P, Yamagata T. 1999. A dipole mode in the tropical Indian Ocean. *Nature* **401**: 360–363.

Salby ML, Hendon HH. 1994. Intraseasonal behavior of clouds, temperature, and motion in the tropics. *J. Atmos. Sci.* **51**: 2207–2224.

Shinoda T, Han W. 2005. Influence of the Indian Ocean Dipole on atmospheric subseasonal variability. *J. Climate* **18**: 3891–3909.

Shinoda T, Hendon HH, Glick J. 1998. Intraseasonal variability of surface fluxes and sea surface temperature in the tropical western Pacific and Indian Oceans. *J. Climate* **11**: 1685–1702.

Tomczak M, Godfrey JS. 1994. *Regional Oceanography: An Introduction*. Pergamon.

Valsala V. 2008. First and second baroclinic mode responses of the tropical Indian Ocean to interannual equatorial wind anomalies. *J. Oceanogr.* **64**: 479–494.

Vialard J, Shenoi SSC, McCreary JP, Shankar D, Durand F, Fernando V, Shetye SR. 2009. Intraseasonal response of the northern Indian Ocean coastal waveguide to the Madden–Julian Oscillation. *Geophys. Res. Lett.* **36**: L14606, DOI: 10.1029/2009GL038450.

Waliser DE, Murtugudde R, Lucas LE. 2003. Indo-Pacific Ocean response to atmospheric intraseasonal variability: 1. Austral summer and the Madden–Julian oscillation. *J. Geophys. Res.* **108**: 3160, DOI: 10.1029/2002JC001620.

Wang B, Rui H. 1990. Synoptic climatology of transient tropical intraseasonal convection anomalies: 1975–1985. *Meteorol. Atmos. Phys.* **44**: 43–61.

Wheeler MC, Hendon HH. 2004. An all-season real-time multivariate MJO index: Development of an index for monitoring and prediction. *Mon. Weather Rev.* **132**: 1917–1932.

Wilks DS. 1995. *Statistical Methods in the Atmospheric Sciences*. Academic Press: London, UK.

Woolnough SJ, Slingo JM, Hoskins BJ. 2000. The relationship between convection and sea surface temperature on intra-seasonal timescales. *J. Climate* **13**: 2086–2104.

Woolnough SJ, Slingo JM, Hoskins BJ. 2001. The organization of tropical convection by intraseasonal sea surface temperature anomalies. *Q. J. R. Meteorol. Soc.* **127**: 887–907.

Xie SP, Annamalai H, Schott FA, McCreary JP. 2002. Structure and mechanisms of South Indian Ocean climate variability. *J. Climate* **15**: 864–878.

Zhang CD. 2001. Intraseasonal perturbations in sea surface temperatures of the equatorial eastern Pacific and their association with the Madden–Julian oscillation. *J. Climate* **14**: 1309–1322.

Zhang CD. 2005. Madden–Julian oscillation. *Rev. Geophys.* **43**: RG2003, DOI: 10.1029/2004RG000158.